



## GEOSCIENCES

# Gamma-ray spectrometry of the Araguainha impact structure, Brazil: Additional insights into element mobilization due to hydrothermal alteration

EMILSON P. LEITE, JOHANN LAMBERT, MARCOS ALBERTO R. VASCONCELOS,  
ALVARO P. CRÓSTA & ALESSANDRO BATEZELLI

**Abstract:** We present the analysis of airborne and ground gamma-ray spectrometry signatures of the Araguainha impact structure, located in central Brazil, the largest impact structure in South America with ~ 40 km diameter. The airborne data are total gamma-ray counts per second collected along flight lines spaced 1 km apart. The ground gamma-ray data are concentrations of potassium, uranium, and thorium isotopes calculated from radiations measured in three individual channels. The objectives are to distinguish lithologies within the structure, which have naturally distinctive radiogenic signatures, and identify potential post-impact hydrothermal alteration zones, as indicated by high K concentrations. Based on results obtained by numerical modeling of the crater formation, we infer the locations of potential occurrences of target rocks that may have undergone hydrothermal alteration as a result of the impact. The deviations from the background potassium concentration show significant anomalous K values at the center and in the northwestern crater rim, where high concentrations of U are also observed. The numerical model shows that ideal temperature conditions for hydrothermal fluid circulation were attained right after pos-impact gravitational stabilization.

**Keywords:** Araguainha, gamma-ray, geophysics, impact crater.

## INTRODUCTION

Araguainha is the largest impact structure in the cratering record of South America (Crósta et al. 1981, 2019, Theilen-Willege 1981). With a diameter of ~ 40 km, this complex crater was formed in sedimentary shatter cones, planar deformation features (PDFs), and the widespread occurrence of polymictic impact breccia in the central area, including suevite, are the most common products of impact-related deformation in Araguainha. Besides the high hills disposed in a ring-shaped set of ridges around the center of the structure, the overall topography is characterized by circular features corresponding to the inner rings and also to the outer rim, at

~20 km radius from the center, which has the highest elevations on the northwestern region of the structure.

An anomalous concentration of radioactive elements may indicate the occurrence of metamorphic processes, hypogene (hydrothermal) alteration associated with mineralized solutions, supergene alteration, and/or leaching (Ribeiro et al. 2013). Thus, gamma-ray surveys can be useful to map hydrothermal alteration zones associated with mineral deposits, such as Au, porphyry copper, and massive sulfides (e.g., Shives et al. 2003, Airo 2015). Furthermore, many impact craters contain evidence of hydrothermal alteration processes,

such as Chicxulub (Zürcher & Kring 2004, Kring et al. 2020), Sudbury (Mungall et al. 2004), and Bosumtwi (Morrow 2007). In some cases, like the Chicxulub impact structure, it is possible to identify compositional alterations by electrical geophysical methods (Unsworth et al. 2002).

Impact-related processes are known to cause multiple physical and chemical changes in the original rocks. The latter include the remobilization of hydrothermal fluids, directly modifying the composition of the rocks affected by the impact and, hence, of the soils related to these rocks (Vasconcelos et al. 2012, Garcia 2015). Thus, the distribution of radioactive elements has the potential to map these changes, in addition, to characterize the different lithotypes. Several works exemplify the mapping of hydrothermal alteration zones using gamma-spectrometric data, mainly due to the K enrichment in these zones (Moxham et al. 1965, Galbraith & Saunders 1983, Pires 1995, Shives et al. 2003, Zürcher & Kring 2004). The explanation lies in the enormous energy transfer driven by the impact and subsequent shock deformation effects, which promotes physical-chemical changes and creates secondary effects from the release of thermal energy, including hydrothermal alteration. Impact-related hydrothermal systems may last, depending on the size of the crater, up to millions of years (Schneider & Kring 2020). Osinski et al. (2013) claim that over one-third of the terrestrial craters known show evidence of hydrothermal activity derived from impacts.

In this context, this work aims to advance the geophysical knowledge of gamma-ray signatures of impact structures and to distinguish among the radiogenic signature of different geological units within the crater. Additionally, we intend to verify whether the distribution of gamma-ray signatures leads to the identification of possible hydrothermal processes associated with the impact event. Such comprehension may be

helpful to understand how the hydrothermal flow is driven inside the crater system.

Herewith, we explore gamma-ray spectrometry (GRS) data acquired in the Araguainha impact structure, intending to discuss the spatial distributions of radionuclides concentrations ( $^{238}\text{U}$ ,  $^{232}\text{Th}$ , and  $^{40}\text{K}$ ) by analyzing them in terms of lithologies and mineral composition of the rocks. We used numerical modeling of crater formation to support the interpretation of the distributions of radionuclides and established models of hydrothermal processes associated with hypervelocity impacts (Pirajno 2009).

### Geological Setting

The stratigraphic sequences affected by the formation of the Araguainha structure consist of the Paleozoic sedimentary strata of the Paraná Basin, which overlies the Neo-Proterozoic crystalline basement. At the center of the structure, there are rocks from the basement exposed in a near-circular area, namely of the Cuiabá Group, represented by metapelites, followed by a post-tectonic porphyritic alkali granite related to the Pre-Ordovician São Vicente granite (McGee et al. 2012). On top of the crystalline basement, the clastic units of the Paraná Basin, from the Ordovician to the Upper Permian, are exposed in an annular or ring-shaped arrangement, forming a bull's eye pattern. The first ring comprises the Ordovician Rio Ivai Group/Alto Garças Formation, followed by another ring related to the Devonian Paraná Group/Furnas and Ponta Grossa formations, a third ring containing the Carboniferous Tubarão Group/Aquidauana Formation and, closing the bull's eye pattern, the chemical/clastic Passa Dois Group/Irati, and Corumbataí formations. These latter are disposed in a discontinuous ring, outlined by block-faulting (Lana et al. 2007) (Figure 1). The alkali granite has a texture

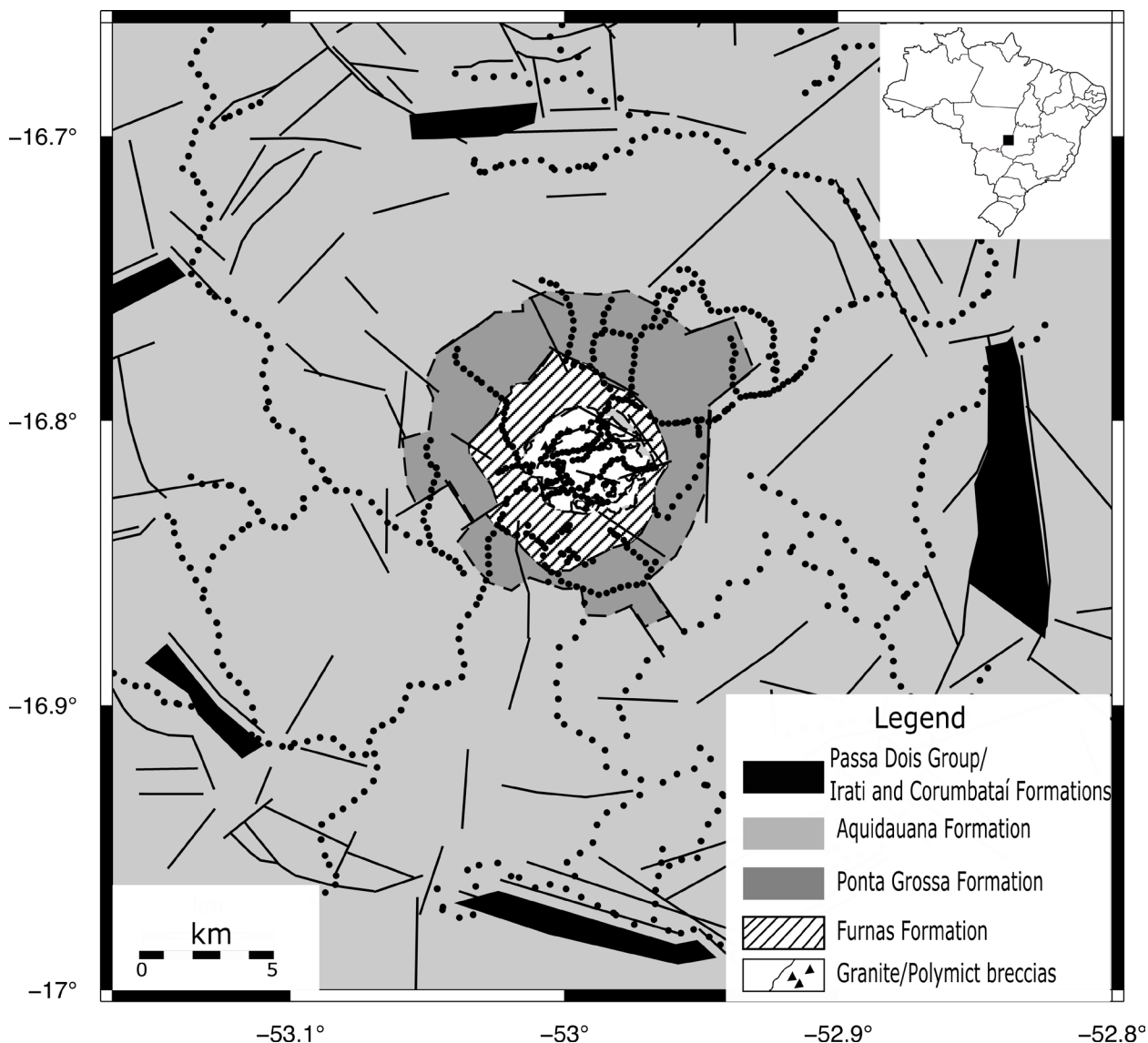


**Figure 1.** Simplified geological map of the Araguainha impact structure. Black dots represent the ground GRS data collected in this research (after Lana et al. 2007).

marked by K-feldspar phenocrysts reaching up to 5 cm. Its primary mineralogy consists of quartz, K-feldspar, albite, biotite, muscovite, and accessories, such as zircon, tourmaline, and calcite (Engelhardt et al. 1992).

Engelhardt et al. (1992) recognized five distinct impactite types in the central part of Araguainha, which are: 1) polymictic breccias; 2) monomictic breccias; 3) granite; 4) melt sheet; and 5) melt veins. The polymictic breccias consist of clasts, from pebbles to boulders, of sedimentary

rocks and subordinate amounts of granite, plus variable amounts of melt, while the monomictic breccias are composed of sandstones from the Furnas Formation (Silva et al. 2016, Engelhardt et al. 1992). Although the formation of melts from shocked rocks is a common process, geochemical analysis indicates that the melt sheets do not significantly contribute from the sedimentary sequences. Machado et al. (2009) proposed that melt sheet was a direct product of the total melting of the granite.

Silva et al. (2016) classified the granite and its products as 1) weakly shocked granite; 2) quartz-rich weakly shocked granite; 3) partially molten granite; 4) melt sheet; and 5) melt veins. These rocks differ in texture, occurrence, and spatial distribution, but their geochemistry indicates similar compositions.

The Alto Garças Formation (Rio Ivaí Group) is constituted by whitish and reddish conglomerates, with predominantly quartz pebbles and a feldspathic sandy matrix. Towards the top, the conglomerate grades fine to medium sandstone, feldspathic, white, and pink, subangular to rounded grains, and very friable. The significant increase in feldspar in the composition of the sandstones at the top of the Alto Garças Formation is represented by the increase in radioactivity in the gamma-ray profiles (Assine et al. 1994).

The Paraná Group strata are composed of the marine conglomerates and sandstone of the Furnas Formation (Lower Devonian) and shales and siltstones with sandstone lenses of the Ponta Grossa Formation (middle and upper Devonian) (Milani 2007). Lana et al. (2007) also observed iron-rich siltstones intercalated with fine-grained sandstone and thin conglomerate lenses within the structure.

According to Melo et al. (2011), the Furnas Formation predominantly comprises quartz sandstones whose original composition ranged from quartz sandstones to subarkose and even arkoses. The current dominance of quartz results from diagenetic processes that transformed the feldspars. The current mineralogy includes, among the detrital minerals, quartz (97%), feldspar (1%), lithic fragments (1%), and micas (1%), in addition to less abundant accessories (Melo et al. 2011). In the lower part of the Furnas Formation, coarse, feldspathic, and kaolin sandstones predominate. Towards the top, the amount of feldspar decreases, with the

predominance of fine, micaceous, and clayey sandstones (M.L. Assine, unpublished data).

The Ponta Grossa Formation consists of gray-to-black shales intercalated with feldspathic sandstones. From a mineralogical point of view, this unit is composed of several phyllosilicates (kaolinite, Illite, muscovite, biotite, and chlorite) ( $\pm 65\%$ ), carbonate (siderite) ( $\pm 20\%$ ), quartz, and detrital feldspar (predominantly microcline) ( $\pm 10\%$ ), iron oxides/hydroxides (goethite and hematite) ( $\pm 5\%$ ) and traces of heavy minerals (tourmaline, zircon, rutile) (Montibeller et al. 2017). In addition, organic matter and levels rich in calcium phosphates (apatite, carbonate, fluorapatite, hydroxyapatite) are very common in this unit, reaching up to 60% (N.G. Christiano, unpublished data).

Sandstones represent a series of petrographic types, among which very fine arkose sandstones predominate, and those with hematite cementation and glauconitic sandstones stand out (Montibeller et al. 2017). They are composed of quartz (54%), detrital microcline ( $\pm 35\%$ ), muscovite (5%), opaque minerals, and iron hydroxides ( $\pm 5\%$ ).

Moving outwards from the central part of the structure, there is the Aquidauana Formation of the Tubarão Group, which is composed, in its basal portion, of iron-rich sandstones alternated with matrix-supported conglomerates. At the top, it has cross-stratified sandstones with laminated siltstones (Lana et al. 2007).

The Aquidauana Formation has many facies, including mudstones, rhythmites, diamictites, sandstones, and conglomerates. One of the main characteristics of this unit is the reddish color given by iron oxide coatings that involve the mineral grains. The mud facies occur in large quantities and are composed of red sandy mudstones (with up to 35% sand) and rhythmites (intercalations of clay and very fine sandstone). A.L.D. Gesicki (unpublished data), based on SEM

and X-ray diffraction data, identified detrital smectite and chlorite, autogenic Illite, and kaolinite as the main clay minerals of these facies. Sandy facies vary in particle size from very fine to coarse-grained and have up to 10% of the clay matrix. The sandstones are polymodal, poor-to-moderately sorted, mainly composed of quartz grains (mono and polycrystalline) and, subordinately, potassium feldspar (up to 10%) and lithic fragments (5 to 7%) A.L.D. Gesicki (unpublished data). Conglomeratic facies are composed of quartz, quartzite, granites, metasediments, and alkaline rock clasts. The clasts are sub-rounded, with diameters ranging from 0.5 to 20 cm (A.L.D. Gesicki, unpublished data).

Stratigraphically above those packages is the Permian Passa Dois Group, containing the Irati and Corumbataí formations. The former has alternating siltstone layers with chert, overlapped by interspersed carbonates and black shales at the top. The latter includes layers of claystone alternated with sandstones, siltstones, carbonate, and small amounts of chert (Lana et al. 2007).

The Irati Formation comprises two distinct facies associations: a lower constituted by siltstone, known as the Taquaral Member, and an upper constituted by carbonate and shales, known as the Assistência Member. At the lower part of the Irati Formation (Taquaral Member), yellow-colored siltstones predominate, with low organic matter content (less than 1%). In comparison, in the upper part of Irati Formation (Assistência Member), organic matter content can reach up to 21% (D. Silva, unpublished data). The carbonates of this unit are dolomitic (J. Hachiro, unpublished data), crypto to microcrystalline, partially replaced by microcrystalline silica, and are classified as dolomitic mudstone (Yamamoto et al. 2004). Gray siltstone layers have submillimeter lamination with alternating

thin light beds composed of quartz, feldspar, muscovite, biotite, and dark beds rich in organic matter. Lamination is predominantly plane-parallel, sometimes lenticular (Yamamoto et al. 2004). Shales rich in organic matter occur throughout the upper portion of the Irati Formation, either as continuous layers or as rhythmic intercalations in carbonates. These shales are formed by smectite (70%), Illite (30%), and chlorite traces (Yamamoto et al. 2004).

According to Christofolletti et al. (2015), the Corumbataí Formation consists of purple and red siltstones and shales with very fine to medium sandstone lenses. The minerals identified by X-Ray Diffractometry belong to the groups of oxides, carbonates, and silicates. Quartz is the most abundant mineral, followed by microcline and albite. Finally, carbonates are represented by calcite and dolomite and occur in the rock matrix or the form of veins and nodules. The illite, kaolinite, and montmorillonite phyllosilicates represent the unit's most abundant group of clay minerals. Illite means the dominant clay mineral, while kaolinite occurs in smaller amounts, followed by montmorillonites. Additionally, hematite occurs in the form of cutans and cement, responsible for the red color of the deposits.

## MATERIALS AND METHODS

### GRS Airborne data

The airborne GRS map was obtained from a public dataset of the Brazilian Geological Survey (Alto Garças Project - CPRM 1971). The gamma-ray scintillometer used was a single 400 in<sup>3</sup> thallium-activated sodium iodide crystal. The flight lines were NS-oriented and spaced 1 km apart. The flight height was about 100 m. The atmospheric radioactive background was detected by flying at about 800 to 1000 m above the ground, where the sensor was isolated

from the radioactive geological influence. Suppression of the radioactivity due to air humidity and rain was monitored by flying over specific predefined profiles after any rainfall. Altitude corrections were applied by fitting an exponential model that connected total radiation count to flight heights. The input data for this model were acquired from 12 flights over an anomalous zone with heights varying from 90 to 450 m while maintaining the same speed and flight orientation. The atmospheric pressure

absorption coefficient determined from this fitting was  $0.0056 \text{ m}^{-1}$ . The data was then reduced to a common predefined height of 120 m above ground. The CPRM report contains only a PDF file with a contour map and 65 profiles of the total gamma-ray count along flight lines. These profiles were digitized at approximately every 80 m, totaling ~34000 digitized points that were interpolated in regular grid with cell size of 150 m x 150 m (Figure 2a).

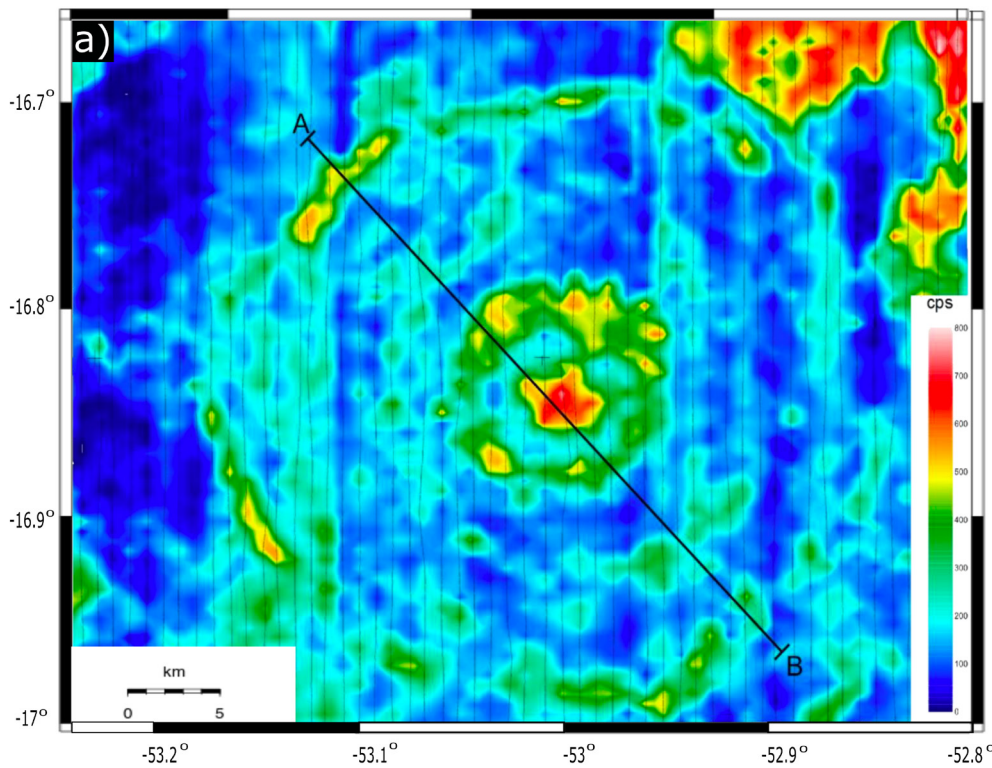
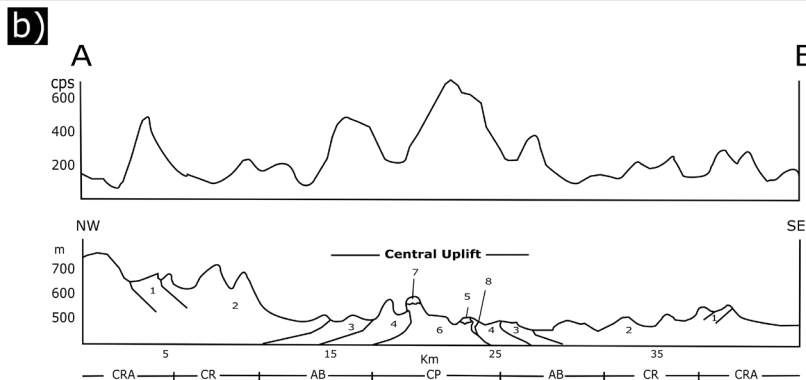


**Figure 2. (a)** Total gamma-ray count in cps for the whole structure of Araguinha (airborne data from Alto Garças Project-CPRM 1971). The thin black vertical lines correspond to the flight lines. **(b)** Total gamma-ray count extracted along the A-B profile and corresponding geological profile. 1- Passa Dois Group; 2- Aquidauana Formation; 3- Ponta Grossa Formation; 4- Furnas Formation; 5- impact melt; 6- granite; 7- Polymictic breccia; 8- Phyllite. Labels correspond to CRA: crater rim area; CR: crater ring; AB: annular basin; CP: central peak (after Yokoyama et al. 2012).



### GRS ground data

The ground GRS data was collected using a portable RS-230 gamma-ray spectrometer with a sensor composed of a bismuth germanate scintillation crystal (Radiation Solutions 2008). The complete dataset is available in the Zenodo public repository (Lambert et al. 2020). The spectrometer measures total counts per second (cps) and cps for energy channels of  $^{40}\text{K}$ ,  $^{232}\text{Th}$ , and  $^{238}\text{U}$  with peaks at 1.46 MeV, 2.62 MeV, and 1.76 MeV, respectively. Gamma-rays are detected within the energy range of 30 keV – 3 MeV, and a maximum of 65,535 counts can be registered for each measurement. This equipment calculates concentrations of K (%) and equivalent concentrations of Th (ppm) and U (ppm) automatically, based on calibration equations built by the manufacturer into the instrument.

At each location, we collected radiation measurements during 120 s to allow sufficient time for calibration. The device integrates the counts over an area of ~1 m diameter and a depth of ~25 cm when it is in direct contact with the material (Erdi-Krausz et al. 2003). It is important to note that the detector assumes a homogeneous half-space around the target material. Stripping and background corrections were automatically calculated based on numerical coefficients provided by the manufacturer (Radiation Solutions 2008). Three portable concrete pads of 1 m × 1 m × 30 cm with known potassium, uranium, and thorium concentrations were used to determine the stripping coefficients applied to gamma-ray counts to convert them to each element concentration. A fourth pad without the three elements was used to determine the background coefficient (Grasty et al. 1991). We used a portable Garmin Etrex 30 GPS for spatial positioning.

Measurements were done mainly on rock outcrops. However, due to the high degree of

weathering, we also measured on soil to obtain a more homogeneous distribution of data points. After removing spurious values, we then analyzed and processed a total of 930 data points (black dots in Figure 1).

We interpolated each channel in a 100 × 100 m regular grid using curvature splines with a tension factor of 0.25 (Smith & Wessel 1990). The profiles were extracted from each individual channel for further analysis (Figure 3). Additionally, a ternary map was produced after normalizing the grids, according to the following normalization equations:

$$K = \left( K + U + \frac{Th}{4} \right) \quad (1),$$

for potassium, and

$$Th = \frac{\frac{Th}{4}}{\left( K + U + \left( \frac{Th}{4} \right) \right)} \quad (2),$$

for uranium (Erdi-Krausz et al. 2003).

We have calculated K deviations ( $K_d$ ) using the technique described in Saunders et al. (1987). This technique is frequently used to enhance areas with hydrothermal alteration (Pires 1995, Vasconcelos et al. 2012).

### Numerical

We compared the GRS products with temperature values obtained from a numerical model generated using the iSALE shock physics hydrocode (Ivanov et al. 1997, Wünnemann et al. 2006), which is based on the Simplified Arbitrary Lagrangian-Eulerian code (Amsden et al. 1980). To calculate the thermodynamic state of the materials we used the Tillotson EoS (Tillotson 1962) with the temperature extension by Ivanov et al. (2002). Parameter estimation of the model was calculated based on several

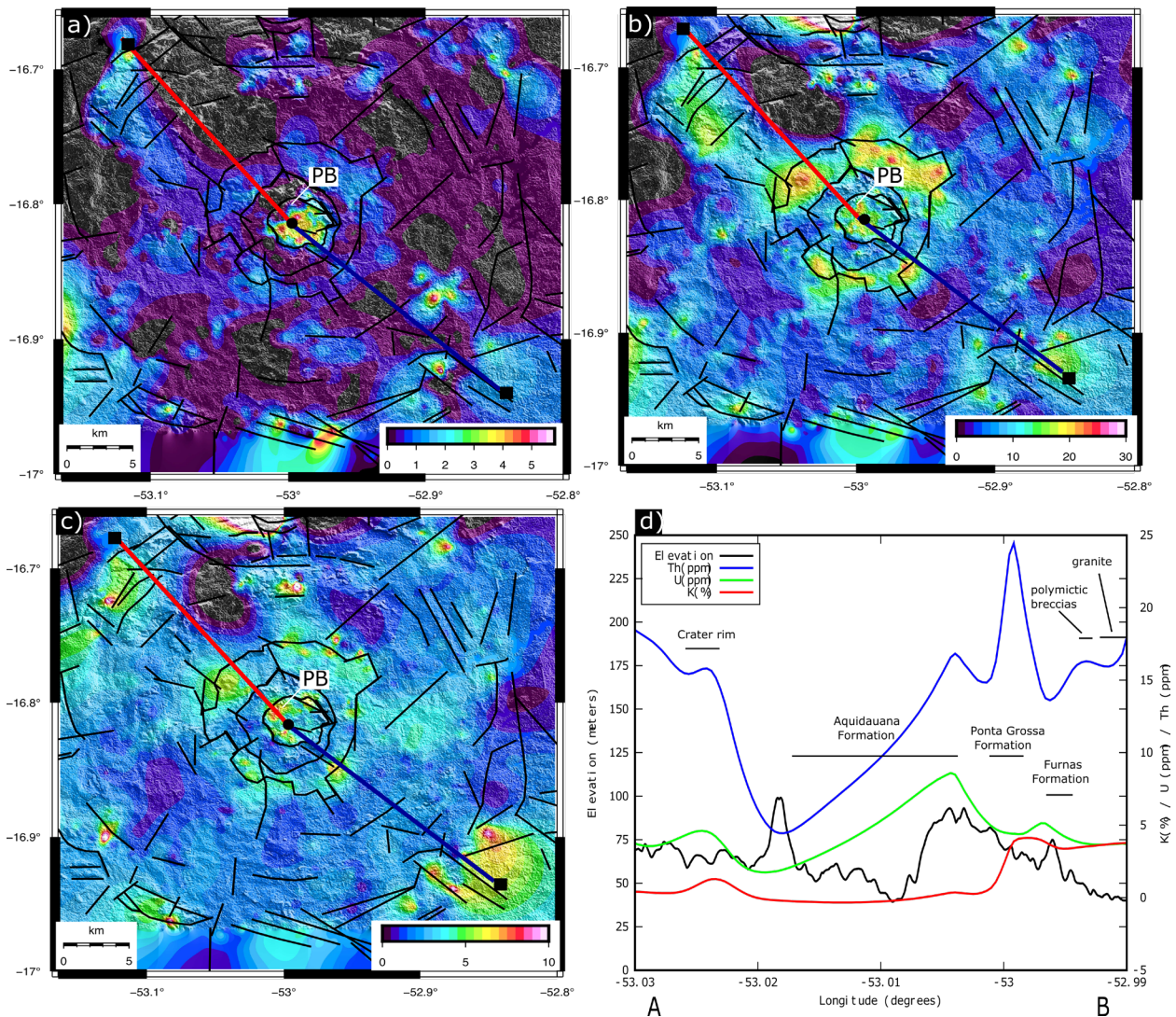


**Figure 3.** Gamma-ray individual channels of Araguainha showing the signatures of all three elements draped on a digital elevation model. (a) K channel in %, (b) Th channel in ppm, (c) U channel in ppm. All channels have shown a distinguished signature of the central uplift region. (d) Profile showing the relationship between topography and radio elements in distinctive colors (red line: K; green line: Th; blue line: U; black line: topography). Thin black lines in Figures 3a-3c mark the boundaries between the rock type in the central portion of the structure: granite, Furnas and Ponta Grossa formations, and geological lineaments. Note a distinctive signature of the area comprising polymictic breccias (PB), according to Lana et al. (2007). The blue and red lines in figures 3a, 3b, and 3d correspond to the lines from where radiometric data was extracted. The same lines are shown in Figure 4b.

iterations of the code. The process starts with the contact between the projectile and the target, followed by the shock wave propagation and the associated flow field. The simulation is completed when the gravity-driven motions end in isostatic equilibrium, and the main dynamic movements ceased (Wünnemann & Ivanov 2003).

The computation of the model was constrained by parameters such as topography, diameter, outcropping strata, and layer thicknesses. A stony projectile and two geological superposed superposed geological layers that represented the target rocks were set: the first layer representing the sedimentary package, from the surface to ~1850 m depth (Schneegg &

Fontes 2002, Miyazaki et al. 2021), and the second layer representing the crystalline (granitic) basement.

The analytical equation of state (Thompson & Lauson 1972) for basalt (Pierazzo et al. 1997) and quartzite (Melosh 2007), and a porosity compaction model (Wünnemann et al. 2006), were used to model the thermodynamic behavior of the target rocks. Moreover, using the acoustic fluidization model (Melosh 1979, Wünneman & Ivanov 2003), we introduced the temporary weakening of target rocks during crater formation. The rheology of acoustically fluidized rock is defined by the viscosity  $h$  and the decay time  $T_{dec}$ . Both describe how long the viscous state of the material lasts until seismic shaking has been attenuated. For the work presented here, we have used the results concerning the final temperature of the crater after gravitational stabilization.

## RESULTS

The airborne GRS data show outstanding circular patterns, which allows us to distinguish different areas of the structure (Figure 2a) and relate them to the bedrock geology. There is a circular area of high total counts ( $> 500$  cps) of about 4-5 km-diameter at the center of the structure. This area is surrounded by a low total count ( $\sim 200$  cps)  $\sim 2$  km-width ring, which is surrounded by a thin internal ring with intermediate to high values (400 – 600 cps). Surrounding the central uplift, there is an extensive area ( $\sim 10 - 12$  km) of low counts (up to 300 cps). Finally, the crater rim is clearly marked by intermediate to high cps values (350 – 550 cps) at about 20 km from the center, with just a few areas of lower values.

The section shown in Figure 2b exhibits gamma-spectrometric signatures coinciding with the geological units. The highest peak, of  $\sim 600$  cps, appears over the granitic area. The

Ponta Grossa Formation shows intermediate values with a series of small anomalies of high values similar to those of the Passa Dois group at the crater rim. Furthermore, low values in the central uplift area are associated with the Furnas Formation described above. The Aquidauana Formation also shows low to intermediate values, with a subtle increase in the region of the concentric rings.

Figure 3 presents the individual channels of the gamma-ray ground data, which are consistent with the total count map shown in Figure 2. Intervals corresponding to low, intermediate, and high values for each channel were defined, dividing each color scale roughly into three parts. Thus, the granite appears with high K concentrations ( $> 4\%$ ) at the center of the structure and with an intermediate (10 – 20 ppm) to high (20 – 30 ppm) Th concentrations, and intermediate (3 – 6 ppm) to high (6 – 10 ppm) U concentrations. Additionally, measurements on the eastern part of the granite show a decrease in the gamma signature, despite having been measured on proper rock outcrops. For the granite, we also collected measurements on areas with melt sheet and melt veins exposures, sometimes associated with extremely high values of Th ( $> 30$  ppm). On the other hand, the polymictic breccias of the northwestern portion present low K values ( $< 2\%$ ) (Figure 3a), which turns out to be an effective method to distinguish between the granite and the breccia.

Among the three major lithological types that comprise the central uplift of the Araguinha impact structure (granite, sandstones of the Furnas Formation, and ferruginous siltstones/shales of the Ponta Grossa Formation), the rocks of the Furnas Formation present the lowest concentrations for all channels ( $< 1\%$  of K,  $\sim 12$  ppm of Th and  $\sim 3$  ppm of U; Figure 3). On the other hand, the Ponta Grossa Formation is somewhat highlighted by intermediate to high

concentrations of Th (15 – 25 ppm) and U (3 – 7 ppm) and low concentrations of K (< 2%). As the occurrence of laterites and ferruginous conglomerates characterize the soils directly derived from this unit, they likely correspond to the upper portions of the Ponta Grossa Formation (Lana et al. 2007). Furthermore, this unit contains many siltstones and iron-bearing layers, which may be responsible for the high Th values. As discussed in Dickson & Scott (1997), Iron oxides-hydroxides and clays may retain the Th that was freed by the breakdown of minerals due to the weathering. Also, Th and U may be transported by adsorption on colloidal clays and iron oxides.

Essentially, a decrease of Th and U values and the absence of K characterize the rocks of the Aquidauana Formation in the annular basin (Figure 3d). On the other hand, the rocks of the

Irati/Corumbataí Formations were highlighted only in some areas, by intermediate Th and U values, especially in the crater's rim, with values around 18 and 5 ppm respectively (Figures 3b-d).

In the ternary gamma-ray map draped over the digital elevation model (Figure 4a), it is evident that the innermost area of the central uplift, comprised essentially of granite and polymictic breccias, pink/orange to white colors indicate high levels of the three radiometric elements, with a higher contribution of K in some specific areas. Unfortunately, it is not possible to identify neither the melt sheets nor monomictic sandstone breccias based on the data available due to the data resolution. Also, those rocks are not presented in the geological map used as our reference (Lana et al. 2007). Surrounding this region, the topography is steeper and has the highest elevations, with mountains supported by

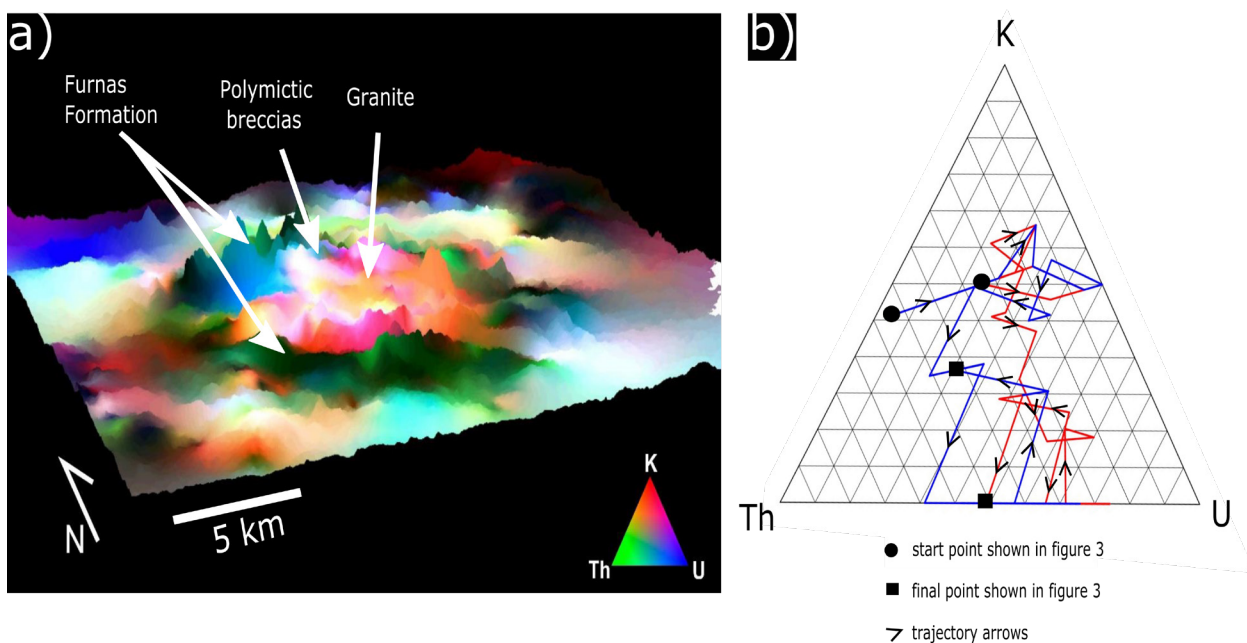


**Figure 4. (a)** Three-dimensional perspective view showing the ternary RGB image superimposed on the Aster DEM with 90 m spatial resolution (Vertical exagertation is 10x). Notice the green circular pattern highlighting the rocks of the Furnas Formation and a high concentration of K in the innermost area **(b)** Ternary diagram with vectors representing the variations of K, Th, and U, starting at the crater rim towards the center, along with the profiles, shown in Figure 3. Concentration intervals are:  $0 < K(\%) < 60$ ;  $25 < Th(\text{ppm}) < 65$ ;  $30 < U < 65$ . Black circles represent the starting point (rim), and black squares represent the final point (center) (see Figure 3). The arrows point out the trajectory of the elements. Both profiles show loss of K outwards.

sandstones belonging to the Furnas Formation, especially in the northern and northwestern areas. Additionally, colors vary from green to blue, emphasizing the occurrence of Th and U, but in relatively lower concentrations. Light colors and smooth relief are associated with the Ponta Grossa Formation.

Additionally, we extracted two radial profiles from the concentration maps of Figures 3a-c, starting at the center of Araguinha and going

outwards, and normalized all values by applying the normalization equations. Figure 4b shows a ternary diagram with vectors representing the radiometric variation from the center outwards for both profiles. The analysis suggests that either the rocks of Araguinha underwent a loss of K from the center outwards or enriched in K inwards.

The  $K_d$  map shows most areas with low to medium values (between -1 and 1) (Figure

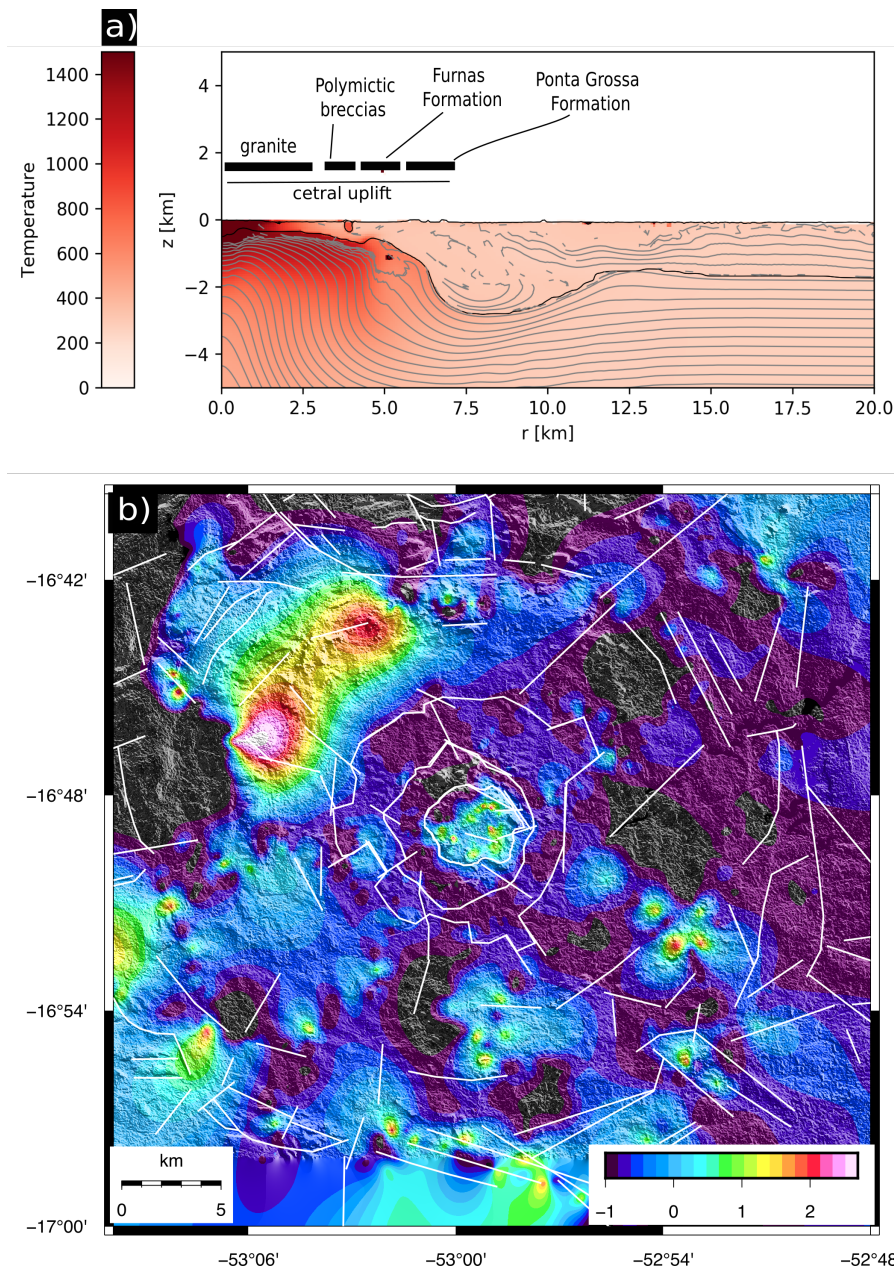


**Figure 5. (a)  $K_d$  map for the entire structure indicates the potential hydrothermalism areas. Notice the concentration of higher values coinciding with the granite outcrops and the two areas in the NW portion of the structure, where exploration activities for U were conducted in the 1970s (b) A section from the last stage of the numerical model, when the crater reached gravitational stabilization; it shows the range of temperatures (in K) attained for half the structure. The central area presents temperature peaks that are possibly related to melting formation from the granite and are responsible for fluid remobilization that produced higher gamma-ray anomalies inwards.**

5a). However, in the central (granite) and northwestern regions (rings and crater rim),  $K_d$  values higher than the background level are observed, which might be related to the occurrence of hydrothermal alteration. Furthermore, the  $K_d$  map also points out that the polymictic breccias of Araguainha have a clear distinctive composition compared to the granitic core.

Finally, the numerical model is presented in terms of the distribution of temperature (Figure 5b). We have chosen only the last frame, which shows the moment when the crater reached gravitational stabilization. The result shows that after its stabilization, the whole crater is still heated due to the shock process, and its temperature increases from the crater rim inwards.

## DISCUSSION

The airborne data shows high values outside the Araguainha structure, crater rim, annular rings, and central uplift. In addition, the Ponta Grossa Formation rocks are highlighted outside and inside the structure, more specifically in the central uplift (Figure 2a). According to Lana et al. (2007), in such areas, the Ponta Grossa Formation comprises iron-rich siltstones, which might be appropriate to adsorb Thorium and Uranium ions. Similarly, the rocks of the Ponta Grossa Formation of the central uplift also present high values in the ground data of the Th channel, which are also highlighted due to the same reasons aforementioned.

Two main factors can produce anomalous concentrations of radiogenic elements in specific parts of impact structures. The first and most important one is derived directly from the host rocks or their erosion and weathering products, leading to the remobilization of such elements (Dickson & Scott 1997). The other factor is related

to the high temperatures and fluid flow (as described by Pirajno 2009) that the target rocks underwent during the crater formation process, especially near its center. These conditions are usually responsible for the chemical alteration of minerals, which can be detected by GRS data if they carry radiogenic elements.

The most acceptable model of the hydrothermal process in impact craters establishes two stages: one phase with higher temperatures (probably 500 – 600 °C), in which mineral reactions result in the formation of K-feldspar and/or albite; the other with temperatures < 500 °C, in which a flow of hydrothermal fluids is dominantly fracture-controlled, and the thermal energy is provided by the hot rocks of the central uplift (Pirajno 2005).

In the beginning, Araguainha had all the necessary conditions for the concentration of radiogenic elements by hydrothermal fluid flow. It has K-bearing basement granite, which was exposed after the formation of the central uplift. According to our numerical simulations, the rocks of Araguainha attained ~1400 K (> 1000 °C) at the end of the crater formation process (Figure 5b). This temperature corresponds to the lower limit of melt assumed to be formed by thermal energy, similar to magmatic rocks (e.g., Carpozen et al. 2005, Koch et al. 2012).

The combined thermal effects result in a variety of phenomena, from partial melting to high-temperature metamorphism and hydrothermal fluid flow (Pirajno 2005). Numerical simulations of hydrothermal activity also demonstrate that the center of an impact structure is the warmer area and the most favorable place for the circulation of hydrothermal fluids (Christou & Bach 2018).

The very high  $K_d$  value in the NW rim is where Nuclebras (1979) prospected U in the late 1970s. Their interpretation was that the Permian strata,

particularly the silexites and pink siltstone of the Corumbataí Formation, hosted the U mineralization. The highest U values were where the strata were more intensely folded and near the fault plane that formed the grabens. They also concluded that the U mineralization was related to the impact's deformation because the highest U values were near the fault planes. One hypothesis is that there was a significant amount of hydrothermal alteration in these rim grabens. This alteration concentrated the U that was already in the strata of the Corumbataí Formation, plus some U that may have flowed from the other strata, from the center outwards.

## CONCLUSIONS

The GRS data of the Araguainha impact structure shows that breccias do not contain radiogenic K, although they are found surrounding the granite. The central uplift area typically receives the most contribution from hydrothermal fluids, which might have carried radiogenic elements inwards, resulting in less radiogenic K available for the other lithologies. This interpretation is based on the  $K_d$  method, which shows anomalous values at the center and in the northwestern rim. The numerical model shows that the crater had ideal temperature conditions for the circulation of hydrothermal fluids after gravitational stabilization. Therefore, our results lead us to infer that the enrichment in certain elements, such as K in certain areas within the crater, may have occurred due to hydrothermal processes related to the formation of the Araguainha structure. As a follow-up, we will compare these results with those from hydrothermal numerical modeling that will allow us to infer fluid mobilization and their association with the high radiometric concentrations in the center of the structure.

## Acknowledgments

The authors thank the following institutions for their financial support: Coordenação de Aperfeiçoamento de Pessoal de Nível Superior – Brazil (CAPES) - Finance Code 001; grant #2016/16021-5, Fundação de Amparo à Pesquisa do Estado de São Paulo (FAPESP). A.P. Crósta acknowledges financial support through a CNPq (Conselho Nacional de Desenvolvimento Científico e Tecnológico) research grant (#302679-2018-9). The ground GRS dataset is available at ZENODO repository (<http://doi.org/10.5281/zenodo.3979695>) under the Creative Commons Attribution 4.0 International License. The dataset is stored in a single spreadsheet file containing coordinates, date and time of measurements, concentrations of the radiometric elements, and derived quantities for geological interpretation and short geological descriptions.

## REFERENCES

- AIRO M. 2015. Geophysical signatures of mineral deposits types-synopsis. Geological Survey of Finland, Special Paper 58, 9-70.
- AMSDEN AA, RUPPEL HM & HIRT CW. 1980. SALE: Simplified ALE computer program for fluid flow at all speeds: Los Alamos National Laboratory, New Mexico, 101 p. doi: 10.2172/5176006.
- ASSINE ML, SOARES PC & MILANI EJ. 1994. Sequências Tectono-Sedimentares Mesopaleozóicas da Bacia do Paraná, Sul do Brasil. *Rev Brav Geociê* 24(2): 77-89.
- CARPOZEN L, GILDER SA & HART RJ. 2005. Paleomagnetism of the Vredefort meteorite crater and implications for craters on Mars. *Nature* 435(7039): 198-201.
- CHRISTOFOLETTI SR, BATEZELLI A & MORENO MMT. 2015. Caracterização Geológica, Mineralógica, Química e Cerâmica da Formação Corumbataí nos Municípios de Tambaú, Porto Ferreira e Santa Rosa do Viterbo – SP, visando aplicação e diversificação de produtos no Polo Cerâmico de Santa Gertrudes. *Geociências* 34(4): 768-783.
- CHRISTOU E & BACH W. 2018. Post Impact Hydrothermal activity. Thermodynamic simulations on the Chicxulub crater and Habitability assessment, European Planetary Science Congress 12: EPSC2018-1175-1.
- CPRM. 1971. Brazilian Geological Survey, Projeto Alto Garças - 1:1000.000. Available in <http://rigeo.cprm.gov.br/jspui/handle/doc/4320>.

- CRÓSTA AP, GASPAR JC & CANDIA MAF. 1981. Feições de metamorfismo de impacto no Domo de Araguainha. *Braz J Geo* 11: 139-146.
- CRÓSTA AP, REIMOLD WU, VASCONCELOS MAR, HAUSER N, OLIVEIRA GJG, MAZIVIERO MV & GÔES AM. 2019. Impact cratering: The South American record – Part 1. *Chemie der Erde* 79: 1-61.
- DICKSON BL & SCOTT KM. 1997. Interpretation of aerial gamma-ray surveys- adding the geochemical factors. *AGSO J Aust Geol Geophys* 17: 187-200.
- ENGELHARDT WV, MATTHÄI SK & WALZEBUCK J. 1992. Araguainha impact crater, Brazil. 1. The interior part of the uplift. *Meteoritics* 27: 442-457.
- ERDI-KRAUSZ G, MATOLIN M, MINTY B, NICOLET JP, REFORD WS & SCHETSELAAR EM. 2003. Guidelines for radioelement mapping using gamma-ray spectrometry data: also an open-access e-book. International Atomic Energy Agency (IAEA).
- GALBRAITH JH & SAUNDERS DF. 1983. Rock classification by characteristics of aerial gamma-ray measurements: *J Geochem Explor* 18: 47-73.
- GARCIA DD. 2015. Caracterização gamaespectrométrica de Cerro do Jarau/RS. Trabalho de Conclusão de Curso. Bacharelado em Geologia, Universidade Estadual de Campinas, 49 p. (Unpublished).
- GRASTY RL, HOLMAN PB & BLANCHARD YB. 1991. Transportable calibration pads for ground and airborne gamma-ray spectrometers. *Geological Survey of Canada, Paper* 90-23: 25.
- IVANOV BA, DENIEM D & NEUKUM G. 1997. Implementation of dynamic strength models into 2D hydrocodes: Application for the atmospheric breakup and impact cratering. *Int J Impact Eng* 17: 375-386.
- IVANOV BA, LANGENHORST F, DEUTSCH A & HORNEMANN U. 2002. How strong was impact-induced CO<sub>2</sub> degassing in the K/T event? Numerical modeling of shock recovery experiments. In *Catastrophic events and mass extinctions: Impact and beyond*. Washington D.C.: Geological Society of America, p. 587-594.
- KRING DA ET AL. 2020. Probing the hydrothermal system of the Chicxulub impact crater. *Sci Adv* 6(22): eaaz3053.
- KOCH SA, GILDER SA, POHL J & TREPMANN C. 2012. Geomagnetic field intensity recorded after impact in Ries meteorite crater. *Geoph J Inter* 189(1): 383-390.
- LAMBERT J, LEITE EP & VASCONCELOS MAR. 2020. Ground Gamma-ray Spectrometry Data of the Araguainha Impact Structure [Data set]. Zenodo doi: 10.5281/zenodo.3979695.
- LANA C, SOUZA FILHO CR, MARANGONI YR, YOKOYAMA E, TRINDADE RIF, TOHVER E & REIMOLD WU. 2007. Insights into the morphology, geometry, and post-impact erosion of the Araguainha peak-ring structure, central Brazil. *Geo Soc Am Bul* 119: 1135-1150.
- MACHADO RA, LANA C, STEVENS G & SOUZA FILHO CR. 2009. Generation, mobilization, and crystallization of impact-induced alkali-rich melts in granitic target rocks: Evidence from the Araguainha impact structure, central Brazil. *Geochim Cosmochim Acta* 73: 7183-7201.
- MCGEE B, COLLINS AS & TRINDADE RI. 2012. G'day Gondwana—the final accretion of a supercontinent: U–Pb ages from the post-orogenic São Vicente Granite, northern Paraguay Belt, Brazil. *Gondwana Res* 21(2-3): 316-322.
- MELO MS DE, GUIMARÃES GB, PONTES HS, MASSUQUETO LL, FIGURIM I, BAGATIM HQ & GIANNINI PCF. 2011. Karst in non-carbonate rocks: Example and implications in the Furnas Formation Sandstones, Campos Gerais do Paraná Region, Southern Brazil. *Espeleo-Tema* 22(1): 81-97.
- MELOSH HJ. 1979. Acoustic fluidization: A new geologic process? *J Geoph Res* 84: 7513-7520.
- MELOSH HJ. 2007. A hydrocode equation of state for SiO<sub>2</sub>. *Meteor & Plan Sci* 42: 2079-2098.
- MILANI EJ, MELO JHG, SOUZA PA, FERNANDES LA & FRANÇA AB. 2007. Bacia do Paraná. In: *Cartas Estratigráficas - Boletim de Geociências da Petrobras* 15(2): 265-287.
- MIYAZAKI MR, LEITE EP, VASCONCELOS MAR, WÜNNEMANN K & CRÓSTA AP. 2021. Bouguer anomaly inversion and hydrocode modeling of the central uplift of the Araguainha impact structure. *An Acad Bras Cienc* 93: e20210081. <https://doi.org/10.1590/0001-3765202120210081>.
- MONTIBELLER CC, ZANARDO A & NAVARRO GRB. 2017. Deciphering the provenance of the Ponta Grossa formation shales in the region of Rio Verde de Mato Grosso and Coxim (State of Mato Grosso, Brazil) using petrographic and geochemical methods. *Geol USP, Sér Cient* 17(1): 41-59.
- MORROW JR. 2007. Shock-metamorphic petrography and microRaman spectroscopy of quartz in upper impactite interval, ICDP drill core LB-07A, Bosumtwi impact crater, Ghana. *Meteorit Planet Sci* 42(4-5): 591-609.
- MOXHAM RM, FOOTE RS & BUNKER CM. 1965. Gamma-ray spectrometer studies of hydrothermally altered rocks. *Econ Geol* 60: 653-671.
- MUNGALL JE, AMES DE & HANLEY JJ. 2004. Geochemical evidence from the Sudbury structure for crustal redistribution by large bolide impacts. *Nature* 429(6991): 546-548.

- NUCLEBRAS. 1979. Resumo mensal do Projeto Domo de Araguainha. Relatório interno, 19, julho 1979.
- OSINSKI GR ET AL. 2013. Impact-generated hydrothermal systems on Earth and Mars. *Icarus* 224(2): 347-363.
- PIERAZZO E, VICKERY AM & MELOSH HJ. 1997. A reevaluation of impact melt production. *Icarus* 127: 408-423.
- PIRAJNO F. 2005. Hydrothermal processes associated with meteorite impact structures: evidence from three Australian examples and implications for economic resources, *Aust J Earth Sci* 52: 587-605.
- PIRAJNO F. 2009. Hydrothermal Processes Associated with Meteorite Impacts. In: *Hydrothermal processes and mineral systems*. Perth: Springer, 1273 p.
- PIRES ACB. 1995. Identificação geofísica de áreas de alteração hidrotermal, Crixás-Guarinos, Goiás, *Rev Bras Geocienc* 25(1): 61-68.
- RADIATION SOLUTIONS. 2008. User's manual for RS-125 Super-spec and RS-230 BGO superspec gamma-ray spectrometer, rev. 1.7. Ontario: Radiation Solutions Inc., Canada, 35 p.
- RIBEIRO VB, MANTOVANI MSM & LOURO VHA. 2013. Aerogamaespectrometria e suas aplicações no mapeamento geológico. *Terrae Didat* 10(1): 29-51.
- SAUNDERS DF, TERRY SA & THOMPSON CK. 1987. Test of National U Resource Evaluation gamma-ray spectral data in petroleum reconnaissance. *Geophysics* 52(11): 1547-1556.
- SCHMIEDER M & KRING DA. 2020. Earth's impact events through geologic time: a list of recommended ages for terrestrial impact structures and deposits. *Astrobiology* 20(1): 91-141.
- SCHNEGG PA & FONTES SL. 2002. Feasibility study of the geoelectric structure of the Araguainha impact, Brazil. *Earth Planets Space* 54: 597-606.
- SHIVES RBK, FORD KL & PETER JM. 2003. Mapping and exploration applications of gamma-ray spectrometry in the Bathurst mining camp, northeastern New Brunswick. In: GOODFELLOW WD, MCCUTCHEON SR & PETER JM (Eds), *Massive sulfide deposits of the Bathurst mining camp, New Brunswick, and northern Maine*. Colorado: Society of Economic Geologists, USA 11: 819-840.
- SILVA D, LANA C & SOUZA FILHO CR. 2016. Petrographic and geochemical characterization of the granitic rocks of the Araguainha impact crater, Brazil. *Meteorit Planet Sci* 51(3): 443-467.
- SMITH WHF & WESSEL P. 1990. Gridding with continuous curvature splines in tension. *Geophysics* 55(3): 293-305.
- THEILEN-WILLEGE B. 1981. The Araguainha impact structure, Central Brazil. *Braz J Geol* 11: 91-97.
- THOMPSON SL & LAUSON HS. 1972. Report SC-RR- 710714: Sandia Labs Albuquerque, New Mexico, 119 p.
- TILLOTSON JM. 1962. Metallic equation of state for hypervelocity impact. General Atomic Report #GA-3216. San Diego, California: Advanced Research Project Agency, 141 p.
- UNSWORTH M, ENRIQUEZ OC, BELMONTE S, ARZATE J & BEDROSIAN P. 2002. The crustal structure of the Chicxulub impact crater imaged with magnetotelluric exploration. *Geophys Res Lett* 29(16): 35-1-35-4.
- VASCONCELOS MAR, LEITE EP & CRÓSTA AP. 2012. Contributions of gamma-ray spectrometry to terrestrial impact crater studies: The example of Serra da Cangalha, northeastern Brazil. *Geophys Res Lett* 39: L043036.
- WÜNNEMANN K, COLLINS GS & MELOSH HJ. 2006. A strain-based porosity model for use in hydrocode simulations of impacts and implications for transient crater growth in porous targets. *Icarus* 180: 514-527.
- WÜNNEMANN K & IVANOV B. 2003. Numerical modeling of crater depth-diameter dependence in acoustically fluidized target. *Planet Space Sci* 51: 831-845.
- YAMAMOTO JK, MONTANHEIRO TJ & HACHIRO J. 2004. Tripoli no Subgrupo Irati: A ocorrência de Ipeúna, Estado de São Paulo. *Rev Bras Geociê* 34(1): 35-40.
- YOKOYAMA E, TRINDADE RIF, LANA C, SOUZA FILHO CR, BARATOUX D, MARANGONI YR & TOHVER E. 2012. Magnetic fabric of Araguainha complex impact structure (Central Brazil): Implications for deformation mechanisms and central uplift formation. *Earth Planet Sci Lett* 331: 347-359.
- ZÜRCHER L & KRING DA. 2004. Hydrothermal alteration in the core of the Yaxcopoil-1 borehole, Chicxulub impact structure. Mexico. *Meteor & Plan Sci* 39: 1199-1221.

#### How to cite

LEITE EP, LAMBERT J, VASCONCELOS MAR, CRÓSTA AP & BATEZELLI A. 2022. Gamma-ray spectrometry of the Araguainha impact structure, Brazil: Additional insights into element mobilization due to hydrothermal alteration. *An Acad Bras Cienc* 94: e20210182. DOI 10.1590/0001-376520220210182.

*Manuscript received on February 5, 2021;  
accepted for publication on October 25, 2021*

**EMILSON P. LEITE<sup>1</sup>**

<https://orcid.org/0000-0003-1691-6243>

**JOHANN LAMBERT<sup>1</sup>**

<https://orcid.org/0000-0003-2483-0503>

**MARCOS ALBERTO R. VASCONCELOS<sup>2</sup>**

<https://orcid.org/0000-0002-4970-0484>

**ALVARO P. CRÓSTA<sup>1</sup>**

<https://orcid.org/0000-0003-0485-1147>

**ALESSANDRO BATEZELLI<sup>1</sup>**

<https://orcid.org/0000-0001-5324-7638>

<sup>1</sup>Universidade Estadual de Campinas, Instituto de Geociências,  
Rua Carlos Gomes 250, 13083-855 Campinas, SP, Brazil

<sup>2</sup>Universidade Federal da Bahia, Instituto de  
Geociências, Departamento de Geofísica, Av. Adhemar  
de Barros, s/n, 40170-110 Salvador, BA, Brazil

Correspondence to: **Emilson P. Leite**

*E-mail: [emilson@unicamp.br](mailto:emilson@unicamp.br)*

### **Author contributions**

Emilson P. Leite: project conception and coordination; data acquisition; data analysis and processing; writing. Johann Lambert: data acquisition; data analysis and processing; geological interpretations. Marcos Alberto R. Vasconcelos: data acquisition; geological interpretations; writing. Alvaro P. Crósta: geological interpretations; writing. Alessandro Batezelli: mineralogical descriptions and writing.

